PHYSICAL REVIEW B **81**, 144412 (2010)

Magnetic vortex dynamics in the presence of pinning

R. L. Compton, T. Y. Chen, and P. A. Crowell*
School of Physics and Astronomy, University of Minnesota, 116 Church Street Southeast, Minneapolis, Minnesota 55455, USA
(Received 4 February 2010; published 9 April 2010)

We have measured the frequency f_G of the gyrotropic mode of a magnetic vortex formed in individual soft ferromagnetic disks with diameters from 600 nm to 2 μm. For low excitation amplitudes, we observe fluctuations in f_G as a function of applied magnetic field. The relationship between the applied field and the spatial displacement of the vortex core from the center of the disk indicates that the fluctuations are due to a distribution of nanoscale defects that pin the vortex core, which has a diameter of $\sim$10 nm. In the limit of high excitation amplitude, the gyrotropic frequency is independent of field, indicating that the core is depinned. In this limit $f_G=f_{ideal}$ where f_{ideal} is the frequency predicted by analytical models and micromagnetic simulations of ideal vortex behavior. We also find both experimentally and in simulations that the average frequency shift $\langle\Delta f\rangle=\langle f_{\max}-f_{ideal}\rangle$ is independent of disk diameter. From this observation we argue that Δf for a particular fluctuation is proportional to the interaction energy W_P of the vortex core with a single nanoscale defect and estimate the average energy to be $W_P/e\approx 2$ eV for the defects in these sputtered permalloy films.

DOI: 10.1103/PhysRevB.81.144412 PACS number(s): 75.78.Fg, 75.75.Jn, 75.75.Fk

I. INTRODUCTION

A magnetic vortex is often the ground state of soft ferromagnetic disks with micron scale diameters and thicknesses $\sim$10 nm. The magnetization curls in the sample plane[1,2] except at the vortex center, in which the out-of-plane magnetization is distributed over a core region that is $\sim$10 nm in diameter.[3,4] The low-frequency dynamics of the vortex state are dominated by the gyrotropic mode, in which the vortex core moves in a circular orbit about its equilibrium position.[5–12] For the ideal vortex, the frequency of the gyrotropic mode f_G is determined by the static magnetic susceptibility χ_m, which is a function of the aspect ratio (diameter over thickness) of the disk.[5,6,9]

The vortex core can be displaced from the center of the disk by application of an in-plane magnetic field.[13,14] In this respect its quasistatic behavior is analogous to domain-wall motion. Domain-wall motion is often accompanied by Barkhausen noise,[15] which is associated with pinning by defects. In bulk materials[16–18] as well as in thin films,[19–22] the sizes of Barkhausen jumps are probabilistic, depending not only on the random distribution of defects in the material but also on the specific configuration of the domain wall. Observation of the Barkhausen effect has recently been extended to individual domain-wall devices, where current- or field-induced domain-wall motion occurs in magnetic wires with widths $\sim$100 nm and thicknesses $\sim$10 nm.[23] In all of these systems, the probability for a jump to occur decays as a power law in the size of the jump. The jump size can be measured as the change in magnetization, or as the area or volume swept out by the propagating domain wall. In principle, the distribution of Barkhausen jumps gives information about the underlying distribution of defects. However, models relating the distribution of jumps to microstructure are complicated by the self-organizing nature of the spatially extended domain wall.[16,24,25]

As in the case of bulk magnetic materials (three dimensional), thin films [two dimensional (2D)], and wires (one dimensional), it has been shown that intrinsic defects can pin the core of a magnetic vortex (zero dimensional) so that the quasistatic motion of the core proceeds in a steplike manner.[14,26] In contrast to a spatially extended domain wall, however, the pointlike nature of the vortex core suggests that its pinning is not a collective phenomenon. This raises the question of whether vortex-core pinning can be used to probe the properties of single nanoscale defects. Such a capability might provide a means to test microscopic models of important macroscopic phenomena such as magnetic hysteresis. In addition, an understanding of the role that vortex-core pinning plays in the motion of domain walls in nanowires is essential to progress toward domain-wall-device applications.[27]

We have previously shown that the presence of intrinsic defects influences the core dynamics, causing the frequency of the gyrotropic mode to fluctuate unexpectedly with applied field as the vortex core moves among the pinning sites.[28] A similar influence on dynamics has been observed in magnetic nanowires in which a vortex domain wall is pinned either by a patterned notch[29,30] or an intrinsic defect.[31] Where domain walls are present, however, it is not always possible to separate domain-wall pinning from core pinning since pinning of the domain wall also contributes to the shift in gyrotropic mode frequency.[32] In this work, we present measurements of the gyrotropic mode frequency of isolated vortex cores as a function of applied field, which provides a means of positioning the vortex core relative to individual pinning sites. Disks were patterned from 50-nm-thick permalloy (Py) films with different crystallographic grain sizes, with diameters ranging from 600 nm to 2 μm. We find that the crystallographic grain size is weakly correlated with the length scale for the pinning landscape sampled by the vortex core but does not influence the average magnitude of the frequency shifts observed. Further, we show that the frequency shift due to pinning is independent of disk diameter, consistent with a model in which the frequency shift gives a measure of the strength of an individual pinning site. We conclude that the pinning interaction between a vortex core and a single defect in our films has an energy $\approx$2 eV. These

TABLE I. Growth parameters for thin permalloy films.

Name	Material	Growth temp.	Rate (Å/s)	Thickness (Å)
SG[a]	Cu	RT	2	300
	Py	RT	1	500
LG[b]	Cu	200 °C	2	300
	Py	200 °C	1	500
XLG[b]	Cu	250 °C	2	350
	Py	200 °C	1	500

[a]Capped *in situ* with 25 Å Al.
[b]Capped with 500 Å SiN after *ex situ* AFM.

observations constrain the possibilities for the physical mechanism of pinning.

II. EXPERIMENTAL CONSIDERATIONS

Crystallographically textured films were grown on commercially polished single-crystal sapphire (Al_2O_3) (0001) substrates with a Cu buffer layer, utilizing a well-known template for the textured growth of transition metals.[33–35] Substrates were sonicated in baths of soap solution (Alconox), deionized water, acetone, methanol, and isopropyl alcohol,[35] and then transferred into a commercial sputtering chamber with a base pressure lower than 3×10^{-7} Torr. Films were grown by dc magnetron sputtering at 100 W in 2.5 mTorr Ar. Data will be presented for three films, which will be referred to as small grained (SG), large grained (LG) and extra large grained (XLG). Growth temperatures and other parameters are given in Table I.

Atomic force microscopy (AFM) images taken in contact mode over 1 μm square regions are shown in Fig. 1 for the three growth temperatures. Multiple, well-separated line cuts through each image were analyzed using a multiple peak fitting algorithm. The grain size for each film is given by the peak separation, averaged over 75 or more peaks. The results, shown as squares in Fig. 1(d), indicate a substantial increase in grain size for growth temperatures above 200 °C. As a check of these values, we have counted the number of grains N in the image area $L^2=1$ μm^2. The average grain diameter $L/\sqrt{N}$ is also shown in Fig. 1(d) and compares favorably to the results based on fits to the line cuts. The roughness for each film was averaged over a 1 μm^2 AFM image using commercial AFM analysis software. The average roughness R_A is defined as

$$\frac{1}{N_iN_j}\sum_{i,j}^{N_i,N_j}|z(x_i,y_j)-\bar{z}|, \quad (1)$$

where z is the surface height, $\bar{z}$ is the average surface height, and the sum is taken over $N_i\times N_j$ image pixels. The average roughness is $R_A=5.7$ Å for the RT film and $R_A=5.6$ Å for the 200 °C film. The much larger grain size of the 250 °C film is accompanied by a large increase in roughness to $R_A=2.24$ nm. In every case, however, the roughness is more than an order of magnitude less than the nominal thickness (50 nm) of the Py layer.

The films were further characterized by wide angle x-ray diffraction. For bulk Cu and Py, we expect (111) diffraction peaks at $2\theta_{Cu}=43.4°$ and $2\theta_{Py}=44.3°$, where θ is the angle between the film normal and the x-ray path. In addition, Al_2O_3 should have a sixth order peak at $2\theta=41.7°$. These peak positions are readily identified in Fig. 2(a), which shows diffraction data for the 200 °C film. The close match

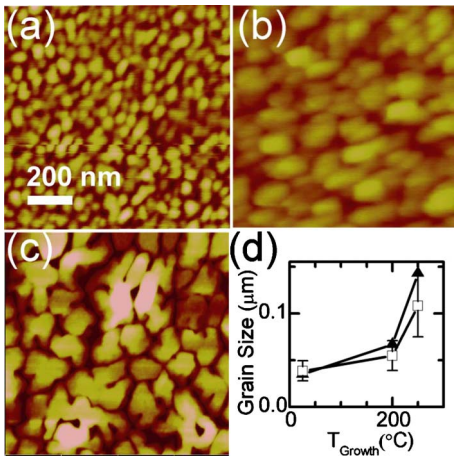

FIG. 1. (Color online) [(a)–(c)] Atomic force micrographs of unpatterned Py films grown at (a) RT, (b) 200 °C, and (c) 250 °C. All images share the scale bar in (a). (d) Grain size versus growth temperature determined by multiple Lorentzian fits to line cuts through the AFM images (open squares). An estimate of grain size is also obtained by counting the number of grains in the 1 μm^2 image (triangles). Error bars give the standard deviation for the fitting procedure.

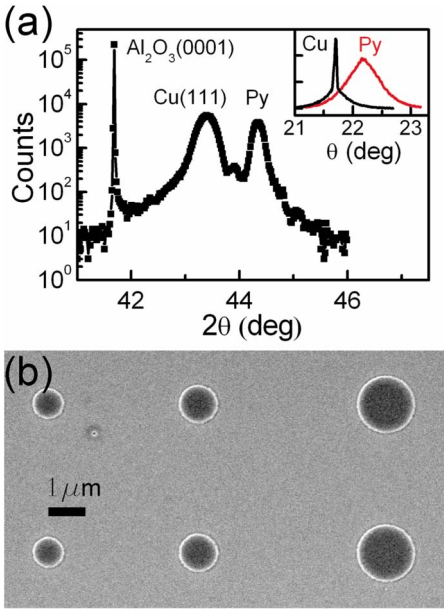

FIG. 2. (Color online) (a) Wide-angle x-ray data for unpatterned Py films grown at 200 °C. Separate rocking curves for the Cu and Py peaks are shown in the inset on a linear scale. (b) SEM of disks patterned by electron-beam lithography and dry etching. The disks shown have nominal diameters of 800 nm, 1 μm, and 1.5 μm.

of the observed lattice constants to their bulk values indicates that the films are relaxed, despite the substantial lattice mismatch with sapphire. Rocking curves for the 200 °C film appear in the inset of Fig. 2. The Cu rocking curve shows a characteristic bimodal distribution. The Py rocking curve, by contrast, is single mode but broad, suggesting poor mosaicity.

Prior to patterning by electron beam lithography (EBL), a 50-nm layer of SiN was reactively sputtered onto the permalloy films. The SiN is used in the dry etching process and also acts as a capping layer for the high-temperature films, which were not capped *in situ*. We use a bilayer resist process with polymethylmethacrylate (PMMA) as the imaging layer and polymethylglutarimide (PMGI) as the undercut layer. Following exposure in a Raith 150 EBL system, the resist is developed in two steps to obtain the image mask (PMMA) and the undercut (PMGI). Dry etching proceeds in three main steps. First, approximately 50-nm Al is evaporated onto the mask and the resist is lifted off. Next, fluorine-based reactive ion etching transfers the Al pattern to the SiN. Finally, the SiN mask is transferred to the metal layer by Ar ion milling. Since the SiN is optically transparent, it can be left as a thick (~50 nm) capping layer. Figure 2(b) shows a scanning electron microscopy (SEM) image of disks patterned from the SG film.

We use time-resolved Kerr microscopy (TRKM) (Ref. 36) to study the vortex-core dynamics in individual magnetic disks. The sample substrate is polished to a thickness less than 30 μm and then positioned above the 30-μm-wide center conductor of a coplanar waveguide, as shown in Fig. 3(a). This mounting technique facilitates the investigation of epitaxial samples since the usual alternative requires deposition directly onto the coplanar waveguide (i.e., polycrystalline metal). The sample is excited by a magnetic field pulse with a temporal width less than 120 ps and amplitude 2–13 Oe (estimate based on the magnitude of the current) oriented in the plane of the disk. A linearly polarized laser pulse (duration 150 fs, $\lambda = 810$ nm) is focused through an oil-immersion objective to a spot with a full width at half maximum (FWHM) ~400 nm. Using the polar Kerr effect, we measure the pump-induced change in the z component of the magnetization as a function of the time delay between the pump and the probe. Typical data are shown in Fig. 3(b). The Fourier transform of the time-resolved data in Fig. 3(c) shows a peak near 5 GHz corresponding to azimuthal spin waves as well as a sub-GHz peak corresponding to the gyrotropic mode.[6,7,10] In the case of an ideal vortex, the frequency of the gyrotropic mode is given by[5]

$$2\pi f_G = k_M / G. \tag{2}$$

The gyroconstant

$$G = 2\pi \frac{L_z M_s}{\gamma} \tag{3}$$

characterizes the vortex core, where L_z is the thickness of the disk, M_s is the saturation magnetization, and γ is the gyromagnetic ratio. k_M is a stiffness due to the magnetostatic energy of the nonequilibrium spin configuration that results

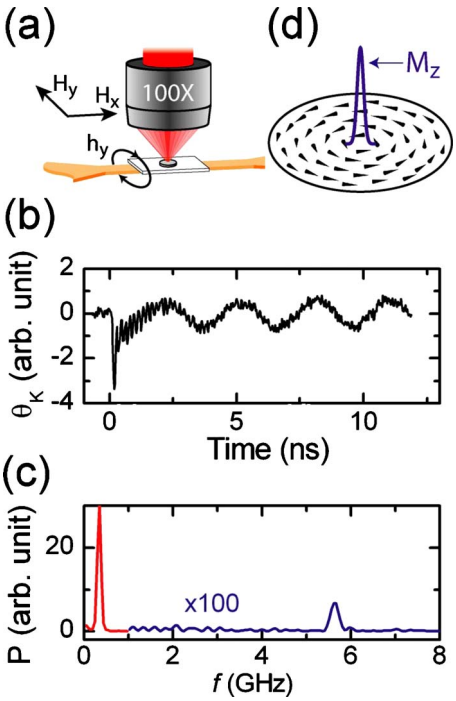

FIG. 3. (Color online) (a) Cartoon of the experimental setup showing the microscope objective focused onto a single magnetic disk, which is mounted on the center conductor of a coplanar waveguide. (b) Representative timescan showing short-lived high-frequency spin waves and the long-lived low-frequency gyrotropic mode. (c) Fourier transform of the time-resolved data showing a spin-wave peak near 5.5 GHz along with the sub-GHz gyrotropic mode. Data above 1 GHz are multiplied by 100 for better visibility. (d) Cartoon of the vortex magnetization distribution, showing the in-plane curling magnetization, along with the out-of-plane magnetization of the vortex core.

when the vortex core is displaced from its equilibrium position. The stiffness is related to the magnetic susceptibility $\chi_M = dM_x/dH_x$ by[5]

$$k_M = \frac{\pi L_z M_s^2 \xi^2}{\chi_M}, \tag{4}$$

where ξ is a constant reflecting the boundary conditions. χ_M is approximately constant for low applied field $H_x < H_{ann}/2$, where H_{ann} is the annihilation field for the vortex core,[26] with a value that also depends on the boundary conditions. The two most common cases considered are the "rigid vortex model" in which the magnetization distribution is presumed to be displaced rigidly in the plane, generating magnetic charges at the boundary of the disk, and the "two-vortex model," in which the vortex deforms so that the boundaries are pole free.[5] (The latter situation can be approximated using the method of images with a second fictitious vortex located outside the disk.) Regardless of the boundary condition, f_G should be constant at low applied field.

During the time that the excitation field pulse (~100 ps rise time) is applied, the sample magnetization experiences a torque $\boldsymbol{M}(\boldsymbol{r}) \times \boldsymbol{h}(t)$. The spatially uniform field pulse $\boldsymbol{h}(t) = h_y(t)\hat{y}$ couples to the x component of the in-plane spins,

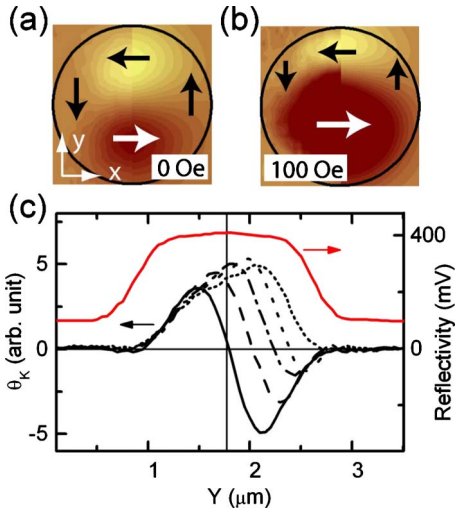

FIG. 4. (Color online) (a) The x component of magnetization as a function of position for a 2-μm-diameter SG disk in (a) zero field and (b) $H=100$ Oe applied in the x direction. The line of nodes gives the Y coordinate of the vortex-core position. The panels are split between experimental images on the left and micromagnetic simulations on the right. (c) Line scans measure Kerr rotation as a function of sample position for a 2-μm-diameter SG disk with the zero crossing giving the location of the vortex core. Line scans are shown for $H_x=0$ (solid line), 50 (dashed), 100 (dash-dotted), 150 (small dashes), 200 Oe (dotted). The solid red curve (right-hand scale) is a line scan of the reflectivity signal.

tilting the magnetization vector in the z direction (out-of-plane). Since TRKM is sensitive to pump-induced changes in M_z, the transient torque due to the excitation field produces a sharp peak in the time-resolved signal that is visible at $t=0$ ns in Fig. 3(b). By fixing the time delay at this peak in the transient torque signal, we can image the spatial distribution of the x component of the magnetization. In the vortex state the x components of the in-plane magnetization have opposite sign above and below the vortex core, as in Fig. 3(d), so that their coupling to the y-directed pump pulse produces z components of magnetization with opposite sign. Figure 4(a) shows a polar Kerr image of a 2-μm-diameter SG disk taken with the time delay fixed at the peak of the pump pulse, demonstrating the expected contrast. The left half of this image is data and the right half is a micromagnetic simulation of the response convolved with a Gaussian of FWHM 400 nm.[37] An image taken in a field of 100 Oe applied in the x direction is shown in Fig. 4(b). As expected, the equilibrium position of the vortex core is displaced in a direction perpendicular to the static field.[13,14] To determine the equilibrium displacement Y of the vortex core from the center of the disk, it is sufficient to obtain vertical line cuts through the 2D images of Fig. 4. Typical line scans are shown in Fig. 4(c) for the 2-μm-diameter disk. The zero crossing, which corresponds to the 2D line of nodes, gives the Y coordinate of the location of the vortex core. To account for drift of the sample position between successive line scans, the reflectivity signal is also monitored, allowing the transient torque signal to be referenced to the spatial profile of the disk.

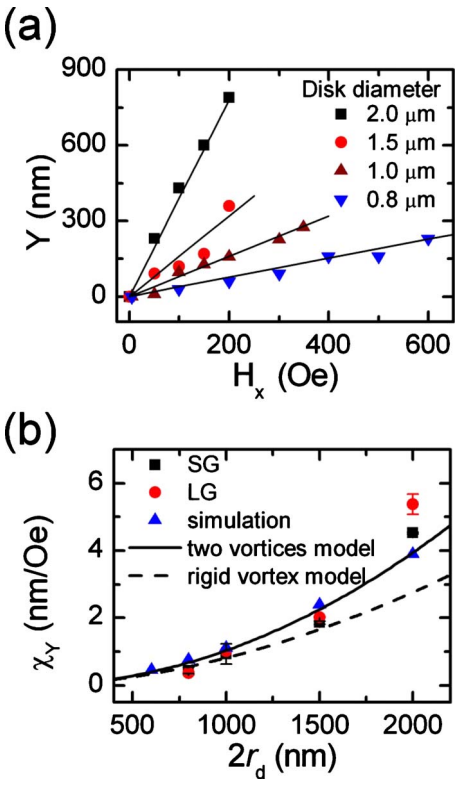

FIG. 5. (Color online) (a) Displacement versus field for four SG disks with different diameters. Displacements are relative to the zero field core positions. (b) Linear fits to the data in (a) give the displacement susceptibility χ_Y versus the disk diameter $2r_d$ for SG disks (squares) and LG disks (circles). Also shown are values of χ_Y obtained from micromagnetic simulations (triangles). The solid line is the analytical calculation based on the two-vortex model and the dashed line is based on the rigid vortex model. Analytical calculations use $M_s=800$ emu/cm^3.

III. RESULTS AND DISCUSSION

A. Displacement susceptibility

We obtained transient torque data by the method of Fig. 4(c) for disks ranging from 800 nm to 2.0 μm in diameter. For small fields, the displacement Y is linear with field H_x, as shown in Fig. 5(a) for a set of SG disks. Linear fits to the displacement curves give the displacement susceptibility $\chi_Y=dY/dH_x$. Typical values are $\chi_Y=4.5\pm0.3$ nm/Oe for the 2 μm SG disk and 0.9 ± 0.2 nm/Oe for the 1 μm disk. In comparison, micromagnetic simulations give 3.9 and 1.1 nm/Oe, respectively. Figure 5(b) shows the measured displacement susceptibilities for both SG (squares) and LG (circles) disks. The overall dependence of χ_Y on disk diameter is approximately quadratic, in agreement with micromagnetic simulations. The agreement with analytical predictions is better for the two-vortex model (no magnetic charges at the disk edges) than for the rigid vortex model, especially for larger diameters.[5,13]

B. Field dependence of the gyrotropic frequency

As discussed in Sec. II, the gyrotropic frequency f_G is proportional to $1/\chi_M$, which is independent of field at small

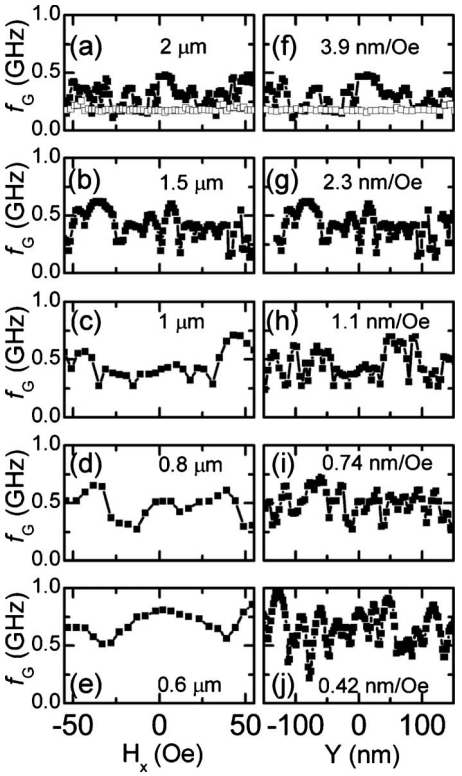

FIG. 6. [(a)–(e)] Field dependence of the gyrotropic frequency for five different SG disks with diameters ranging from 600 nm to 2 μm. Data obtained at pulse amplitudes of 5 Oe are shown as closed squares. Data obtained on the 2-μm disk at a pulse amplitude of 13 Oe are shown as open squares. Plots are labeled with the disk diameter. [(f)–(j)] Frequency data of (a)–(e) versus the displacement $Y=\chi_D \times H_x$. Plots are labeled with the displacement susceptibility χ_Y.

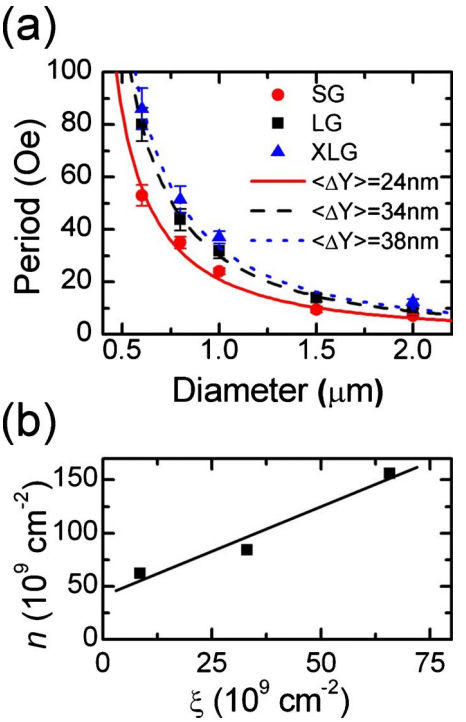

FIG. 7. (Color online) (a) The average period of the gyrotropic frequency fluctuations for disks with diameters ranging from 600 nm to 2 μm. Data are shown for XLG disks (blue triangles), LG disks (black squares), and SG disks (red circles) Solid lines are fits to the data, as described in the text. The displacement period ΔY is the only fitting parameter. (b) Areal defect density n versus areal grain density ξ.

applied fields. We therefore expect only a weak dependence of f_G on static applied field.[9,38] In the present experiment, time scans were taken by focusing the time-resolved Kerr microscope to a point on the surface of a single disk at a radius of 300 nm from the center. The Fourier transforms of the time-resolved data at different values of H_x were fit to Lorentzians to obtain f_G as a function of H_x, shown for a 2-μm-diameter SG disk in Fig. 6(a). For an excitation field of $h_y(t)=13$ Oe (open squares), $f_G=0.18$ GHz, independent of static field. This observed frequency compares favorably with the value of 0.23 GHz obtained from the two-vortex model and the value of 0.21 GHz obtained from micromagnetic simulations. However, for a lower excitation amplitude $h_y=5$ Oe (closed squares), the frequency fluctuates irregularly with field. These fluctuations are repeatable to within 50 MHz for a given disk and are independent of core polarity. The fluctuations are observed in all disks but fluctuations for neighboring disks are uncorrelated. Figures 6(b)–6(e) show the dependence of f_G on static field for SG disks with diameters decreasing from 2 μm to 600 nm. As the diameter decreases, there is an obvious increase in the field scale of the quasiperiodic fluctuations.

Knowledge of the displacement susceptibility $\chi_Y = dY/dH_x$ (see Fig. 5) allows for the conversion of each field scale in Figs. 6(a)–6(e) to a corresponding vortex-core displacement scale in Figs. 6(f)–6(j). The frequency fluctuations for each diameter have approximately the same period ΔY in displacement of the core. In the Lorentz microscopy experiment of Ref. 14, the core moves from defect to defect as the magnetic field is varied. Likewise, in the present experiment, we infer that the movement of the vortex core among point-like pinning sites leads to fluctuations in the gyrotropic frequency. Since different disks fabricated from the same film have an identical areal defect density n, the observed fluctuations are associated with a single length scale, the displacement period $\Delta Y=n^{-1/2}$.

To quantify this observation, the average field separation $\langle \Delta H \rangle$ between frequency peaks was obtained by counting the number of frequency peaks in a given field range. A peak is defined as a local maximum that is comprised of at least two points and averages are taken over approximately 10 peaks for each disk. $\langle \Delta H \rangle$ is shown for each disk diameter in Fig. 7(a). Data are shown as symbols for five different disk diameters patterned from SG (circles), LG (squares), and XLG (triangles) films. Note that $\langle \Delta H \rangle$ increases by approximately a factor of 7 as the disk diameter decreases from 2 μm to 600 nm. We fit the data of Fig. 7(a) using

$$\langle \Delta H \rangle = \langle \Delta Y \rangle / \chi_D, \tag{5}$$

where χ_D is obtained from a second-order polynomial fit to the micromagnetic simulations of Fig. 5. Fits to the data of Fig. 7(a) give $\langle \Delta Y \rangle = 24$ nm for the SG sample, 34 nm for

the LG sample, and 38 nm for the XLG sample. The good agreement of the fitted curves with the data strongly supports the hypothesis that the different periods $\langle \Delta H \rangle$ for the different disk diameters are associated with a single length scale $\langle \Delta Y \rangle$ that is characteristic of the defect density in each Py film. Using the values obtained for $\langle \Delta Y \rangle$, we infer the areal density of pinning defects to range from $n_{SG} \approx 1.7 \times 10^{11}$ cm^{-2} to $n_{XLG} \approx 6.9 \times 10^{10}$ cm^{-2}. As shown in Fig. 7(b), increasing defect density n is correlated with increasing areal density of grains ξ (decreasing grain diameter). This trend is expected for pinning that is associated with grain boundaries, which coincide with changes in microstructure and trapped impurities. We note, however, that the linear fit to the data reveals a substantial offset, indicating the presence of a large population of defects that are not associated with grain boundaries.

C. Statistics

The displacement of the vortex core from one pinning site to another is reminiscent of the movement of a section of a domain wall that escapes from one pinning site and jumps to another. The instantaneous reversal of the magnetization in the region swept across by the domain wall appears as a Barkhausen noise jump in a magnetization measurement. A general feature of Barkhausen noise is a power-law relationship between the size of a Barkhausen jump and the probability for the jump to occur. Power-law behavior is associated with the spatially extended nature of a domain wall[16,25] and is therefore evidence of the collective pinning of a large system by a distribution of pinning sites. In contrast, the magnetic vortex core probes a single defect at any given location. Power-law behavior is therefore not expected for the distribution of jump sizes for a vortex core. We take the separation between frequency peaks ΔH as a measure of the size of a jump since the core displacement is proportional to applied field. Figure 8(a) shows a histogram of the distribution of ΔH from data sets for 1 and 2 μm SG disks, each containing over 100 frequency peaks. Each data set consists of nine different f_G versus H_x sweeps, each taken at a different value of H_y. The value of H_y was increased by 10 Oe for each sweep to ensure that a different region of the sample would be probed. As before, peaks were identified as local maxima comprised of at least two points. The observation of a sharply peaked distribution for ΔH rather than power-law behavior strongly supports the notion that pinning occurs as an interaction between the vortex core and an individual pinning site.

As was done in Fig. 6, we have used the displacement susceptibility χ_D to convert the field scale of Fig. 8(a) to the displacement scale of Fig. 8(b). For both 1 and 2-μm-diameter SG disks, the distribution of jump sizes ΔY overlaps closely. This strengthens the observations of Fig. 7 since not only the mean magnitudes of core jumps but also their distributions are nearly equivalent for different disks fabricated from the same film.

D. Imaging pinning defects

By applying orthogonal in-plane magnetic fields, it is possible to move the vortex core to any point in the disk. The core thereby functions such as a nanoscale scanning probe, as the local value of the gyrotropic frequency is used to map the pinning potential. We have used this approach to scan 1-μm-diameter disks using a pulse amplitude of $\approx$7 Oe. Magnetic fields in the x and y directions are varied in steps of 5 Oe over a range of 100 Oe, which leads to a core displacement over a 110×110 nm^2 spatial region. Figures 9(a)–9(c) show the spatial distribution of pinning sites for 1-μm SG, LG, and XLG disks. The field scale is multiplied by the displacement susceptibility χ_Y to obtain the length scale bar, which is the same for all six panels of Fig. 9. The gyrotropic frequency is represented by a color scale and pinning sites appear as pointlike regions of high contrast separated by a matrix of lower-frequency unpinned behavior. We have previously confirmed that reversal of the vortex chirality rotates the image by 180° since the direction of core displacement depends on chirality.[28] From the areal density of peaks, we confirm that the density of pinning defects is consistent with the results of Fig. 7(b). The representative AFM images of Fig. 1 are shown in Figs. 9(d)–9(f) at a magnification that corresponds to the spatial range of Figs. 9(a)–9(c). Although the density of pinning sites decreases with increasing grain size, we have already noted that there does not appear to be a simple correlation between crystallographic grain structure and the spatial density of pinning sites. In particular, comparison of Figs. 9(c) and 9(f) indicates that the density of defects is much higher than the density of crystallographic grains. The peaks in Fig. 9(c) are

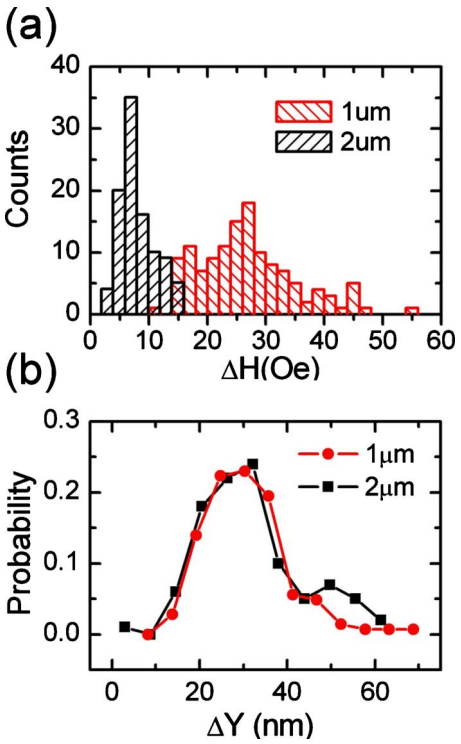

FIG. 8. (Color online) Statistics extracted from data sets containing over 100 frequency peaks, obtained from 1- and 2-μm-diameter SG disks. (a) Histogram showing the distribution of the field separation ΔH between frequency peaks. (b) Probability distribution for the jump size ΔY for 1- and 2-μm disks, obtained from (a) using the relation $\Delta Y = \chi_Y \times \Delta H$.

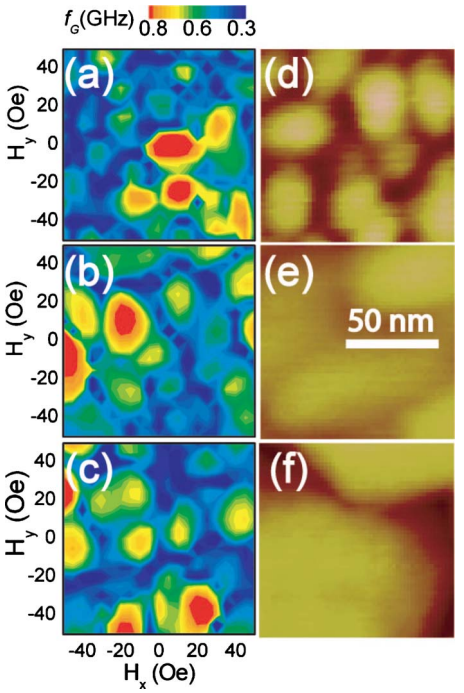

FIG. 9. (Color online) [(a)–(c)] Contour maps of the gyrotropic frequency f_G as a function of static field applied along both in-plane directions for 1-μm-diameter SG, LG, and XLG samples, respectively, obtained at a pulse amplitude of ≈ 6 Oe. f_G is mapped to a color scale so that pinning sites (high frequency) appear as points of high contrast. [(d)–(f)] Representative atomic force micrographs of unpatterned SG, LG, and XLG samples. The magnification of (d)–(f) was chosen so that the length scale bar in (e) applies to all six images.

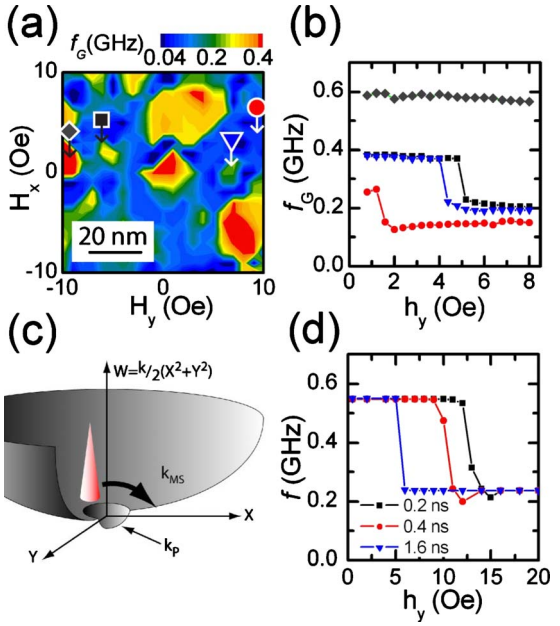

FIG. 10. (Color online) (a) Contour map of f_G versus H_x and H_y for a 2-μm-diameter SG sample, obtained at a pulse amplitude of $h_y \approx 6$ Oe. (b) Gyrotropic frequency versus the amplitude h_y of the excitation pulse. Data were obtained at fixed locations in field space, as indicated by the symbols shown in (a). (c) Cartoon of the potential well with magnetostatic energy W expanded to second order in vortex-core displacement $R^2=X^2+Y^2$. The stiffness k depends on the location of the core. (d) Numerical solution for the model shown in (c). The gyrotropic frequency obtained from simulations of Sec. III F is shown as a function of excitation amplitude for different temporal pulse widths τ of 200 ps (squares), 400 ps (circles), and 1.6 ns (triangles).

approximately the same width as those in Figs. 9(a) and 9(b) but are separated by a greater distance from one another. Although it would be desirable to extract the functional form of the vortex/defect interaction, the displacement susceptibility χ_Y drops significantly when the core is close to a defect, making this difficult. We can, however, estimate the effective range r_p of the pinning potential, assuming that χ_Y approaches its average value as the vortex moves away from the center of the defect. For all three grain sizes, the effective range estimated from the FWHM of the frequency peaks is ~ 20 nm, which is of the same order as the core diameter. This value will be used in Sec. III H in order to estimate the vortex/defect interaction energy.

E. Depinning threshold

In Sec. III B we noted that core dynamics in the high-amplitude regime are field independent, consistent with micromagnetic simulations and analytical theory for the ideal vortex. However, the transition from the low amplitude to high amplitude regime is not well understood.[28] In this section, we examine more closely the depinning transition for several of the frequency peaks of Fig. 10(a), which uses the same method as Fig. 9 to show the distribution of pinning defects near the center of a 2-μm SG disk. Several locations in field space, which maps to real space according to $\chi_D = 3.9$ nm/Oe, are marked with symbols. For each of these locations, data were acquired as a function of the excitation field amplitude h_y.

Figure 10(b) shows the gyrotropic frequency f_G versus h_y. The excitation field was varied by increasing the voltage bias applied to the Auston switch that launches the current pulse into the coplanar waveguide. The amplitude of the current pulse was measured at the 50 Ω input of a high-speed oscilloscope. The peak field at the sample position was then calculated based on the geometry of the coplanar waveguide. For four of the five curves in Fig. 10(b), f_G decreases precipitously at a particular value of h_y. We interpret this sharp decrease in f_G as depinning at a threshold excitation field h_T. At low excitation amplitude, the vortex core remains within the range of a particular pinning site. As the amplitude of the excitation field increases so does the radius of the orbit of the core about its equilibrium position. When the radius of the core's orbit exceeds the range of the pinning potential, the core is depinned and f_G decreases to the frequency predicted by the analytical model of gyrotropic motion.[5] Note that h_T for the data indicated by circles is only ~ 1 Oe. For this location, indicated by the circle in Fig. 10(a), the vortex core is already depinned, since the pulse amplitude used to obtain the data of Fig. 10 was ≈ 6 Oe. On the other hand, for the frequency peak that is indicated by diamonds in Fig. 10(a), we do not observe a corresponding depinning transition in

Fig. 10(b). In this case the largest excitation amplitude achievable in the present setup establishes a lower limit $h_T > 8$ Oe for the expected depinning transition. It is possible to depin all of the defects in the 2-μm disk; however, this requires increasing the pulse amplitude into a regime where changes in the pulse shape make it difficult to characterize the amplitude response of the system.

F. Analytical model

The vortex core is pinned by the position-dependent energy of the core rather than by the collective effect of many defects acting on the entire vortex. This is consistent with the sharply peaked distribution of step sizes in Fig. 8(a). We believe that the energy associated with the in-plane spins outside of the core is nearly independent of the core position. Although small fluctuations of the in-plane anisotropy energy from grain to grain have been proposed as a mechanism of vortex pinning,[14] a mechanism that is associated with the energy of the in-plane spins in the vicinity of the core would seem to be inconsistent with the pointlike contrast in Fig. 9 as well as with the sharp depinning threshold of Fig. 10(b). Here, we propose a phenomenological model in which the position-dependent energy of the core itself gives rise to the observed pinning phenomena.[39,40]

For the ideal case, vortex core dynamics are governed by the Thiele force equation[5,41,42]

$$\mathbf{G} \times \frac{d\mathbf{R}}{dt} - k\mathbf{R} - D\frac{d\mathbf{R}}{dt} = \mathbf{F}(t), \tag{6}$$

where D is a damping constant and $\boldsymbol{F}(t)$ is the time-dependent driving force. It has been shown that solutions of the Thiele equation provide a good description of the gyrotropic mode in permalloy disks.[6,9] Except for the higher frequency, the vortex gyrotropic motion in the pinned case appears to be qualitatively similar to the unpinned regime. We therefore consider the possibility that Eq. (6) also describes the gyrotropic motion of pinned vortex cores but with different effective constants $G=G_M+\Delta G_P$, $k=k_M+\Delta k_P$, and $D=D_M+\Delta D_P$. In each definition, the subscript M indicates the usual contribution due to the magnetostatic properties of the entire vortex while the subscript P refers to a contribution due to pinning of the core. The damping time for the gyrotropic mode exceeds the maximum experimental time delay of 12.5 ns, making it difficult to measure D precisely. We do not observe a correlation of D with the gyrotropic frequency f_G and we therefore assume $\Delta D_P=0$. In order to consider the effect of pinning on the gyroconstant G, it is helpful to consider the more general expression

$$\mathbf{G} = -\frac{M_S}{\gamma}\int d^3\mathbf{r}[\nabla\phi \times \nabla\theta]\sin\,\theta, \tag{7}$$

where θ and ϕ are the polar and azimuthal angles corresponding to the direction of $\mathbf{M}$. There are two important features of the gyrovector that make it only weakly dependent on the pinning potential. First, for any simple vector field that is tangential at the edge of the disk and vertical at the center, $G=2\pi L_z M_s/\gamma$ and will not depend on details of the vortex core size and shape. A second and more subtle fact is that for any defect that reduces the *magnetization* locally, the center of the vortex core will be located at the defect in order to minimize the dipolar energy of the vortex. Since the gradient $\nabla\theta$ vanishes at the center of the core, such defects will therefore leave the value of the gyrovector unchanged. It is likely that any defect large enough or strong enough to modify the gyrovector significantly would also lead to annihilation of the vortex core and complete suppression of the gyrotropic mode. Experimental evidence that G is approximately constant will be presented below and so we will assume that $\Delta G_p=0$. Given these observations we will model the frequency shift due to pinning using an effective spring constant $k=k_M+\Delta k_P$, as illustrated in Fig. 10(c) and assume that the gyroconstant is unchanged.

To implement this model, we have numerically solved the coupled differential equations

$$G\dot{Y} - kX - D\dot{X} + F_x(t) = 0,$$

$$-G\dot{X} - kY - D\dot{Y} = 0, \tag{8}$$

where the x-directed driving force $F_x(t)=M_s\pi\xi R_D L_z h_y(t)$ arises from Zeeman energy that is due to the y-directed excitation field $h_y(t)=h_y^0\exp(-2.73t^2/\tau^2)$. The Gaussian excitation profile has a temporal FWHM τ. For our experimental setup $\tau\approx 200$ ps. At each time step of the numerical integration, the value of k is updated according to the test

$$\text{if } R < r_P, \quad \text{then } k = k_P + k_M,$$

$$\text{else } k = k_M.$$

The results of numerical integration are shown in Fig. 10(d) for $\Delta k_P=1.5k_M$ and $r_P=10$ nm. The factor of 1.5 was chosen to match the observed shift in frequency upon depinning. Results are given for three different values of the temporal width τ of the excitation pulse. In each case, the model reproduces the sharp frequency shift upon depinning, suggesting that the well-defined threshold fields h_T of Fig. 10(b) arise from highly localized, well-separated defects. h_T appears at lower pulse amplitudes as τ increases from the experimentally realistic value of 200 ps to a value of 1.6 ns due to the fact that longer pulses have more spectral power at the natural frequency f_G of the system. Other than shifting h_T, the depinning behavior observed in the frequency response is qualitatively independent of pulse width.

G. Role of the gyroconstant

In general, the amplitude of the motion of the vortex core increases sharply upon depinning, as in Ref. 28. For pulsed field measurements, the amplitude of the core's orbit also depends on the temporal width of the excitation pulse. This can be understood within the model of Sec. III F, which includes four forces. The driving force $\mathbf{F}_x(t)$ due to Zeeman energy and the restoring force $-k_M\mathbf{R}$ due to magnetostatic confinement act mainly on the bulk of the disk while the pinning force $-\Delta k_P\mathbf{R}$ and the gyroforce $\mathbf{G}\times\dot{\mathbf{R}}$ act on the core. Assuming the vortex core is massless (i.e., it does not

change its shape), there is no force term proportional to the acceleration of the core. The instantaneous speed $\dot{R}$ therefore depends only on the rise time of the excitation pulse. For short pulses (relative to the gyrotropic period), such as those in our experiment, this instantaneous speed is large, so that the gyroforce is large relative to the other forces. In this regime, the amplitude of the subsequent gyrotropic motion is determined primarily by the gyroforce and is relatively insensitive to the strength of the pinning potential.

To confirm these statements, we note that for an excitation pulse along the y direction, the driving force due to Zeeman energy is in the x direction. The gyroforce $\boldsymbol{G}\times d\boldsymbol{R}/dt$, however, is perpendicular to the instantaneous velocity and will therefore be primarily in the y direction, parallel to the excitation pulse. The force due to pinning will act as a restoring force oriented toward the center of the pinning site. The regime of short pulse duration should therefore be characterized by initial core motion directed parallel to the excitation field pulse, as observed in Ref. 7. We are able to confirm an initial displacement parallel to the pulsed field by combining two timescans taken on the same 2-μm SG disk. One timescan is obtained with the microscope objective displaced along the y axis of the disk, giving the Y component of the motion of the vortex core. The other timescan is taken with the objective displaced along the x axis, giving the X component of motion. The curve in Fig. 11(a) shows the Y signal versus the X signal, which gives the trajectory of the core. The data are filtered by a moving average over a time scale of 400 ps in order to eliminate the contribution due to spin waves. It is clear that the initial motion of the core has a large component parallel to the y-directed field pulse. The small loop that appears after $t=160$ ps is probably due to the residual contribution of unfiltered spin waves. The initial displacement parallel to the pulsed field is a general feature obtained on multiple disks. Similar behavior is seen in Fig. 11(b), which shows a micromagnetic simulation of a 2 μm $\times 50$ nm disk, excited by a 10 Oe, 150 ps pulse in the y direction. We conclude that our experiment is in the short-pulse duration regime, in which the initial response of the core is dominated by the gyroforce.

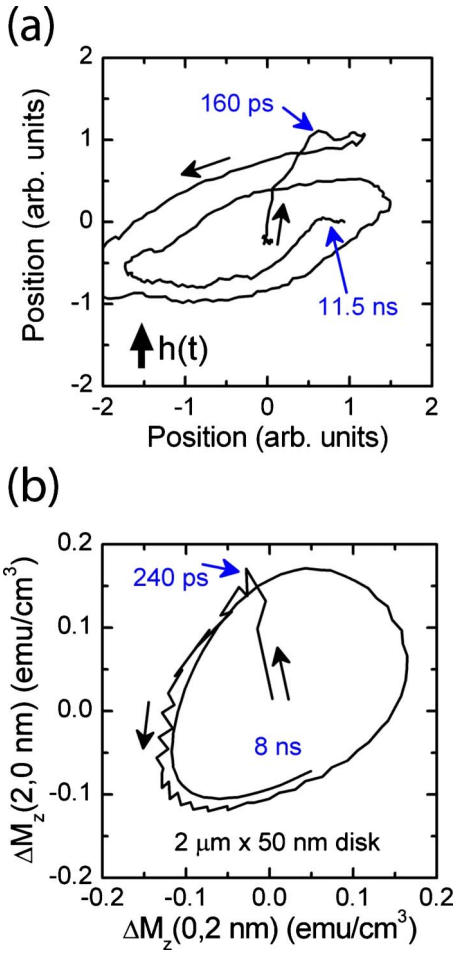

FIG. 11. (Color online) (a) Experimentally observed trajectory of the vortex core, constructed from two timescans that were taken with the objective displaced first along the y axis and then along the x axis of the disk. (b) Simulated trajectory of the vortex core, constructed from simulated timescans obtained at $x=2$ nm and $y=2$ nm relative to the center of the disk.

H. Average frequency shift

We have modeled the effect of pinning as an interaction between the vortex core and a defect that increases the stiffness k of the effective potential. We argued above that the change ΔG_P in the gyroconstant due to pinning is negligible. If this is true then the frequency shift Δf_G due to pinning should be proportional to the pinning stiffness Δk_P. This leads us to a direct estimate of the vortex/defect interaction energy, since $W_P=1/2\Delta k_P r_P^2$, where r_P is the effective range of the harmonic pinning potential. Before estimating W_P, we present the experimental justification for taking $\Delta G_P=0$. Beginning with Eq. (2) the variation in gyrotropic frequency due to variations in stiffness and gyroconstant is

$$2\pi\Delta f_G = \frac{k_M+\Delta k_P}{G_M+\Delta G_P} - \frac{k_M}{G_M}, \tag{9}$$

where Δk_P and ΔG_P account for the effects of pinning within the Thiele model, as described above. We expand Eq. (9) to first order in ΔG_P

$$2\pi\Delta f_G \approx \frac{\Delta k_P}{G_M} - \Delta G_P \frac{k_M+\Delta k_P}{G_M^2}. \tag{10}$$

We note that k_M, the stiffness due to the magnetostatic energy of the disk, depends on disk diameter, while G_M does not. Therefore, the relative contributions of Δk_P and ΔG_P to the frequency shift in Eq. (10) can, in principle, be extracted from the dependence of Δf_G on disk diameter. Experimentally, we define the frequency shift Δf_G as the difference between a local maximum in frequency $f_{\max}$ and the gyrotropic frequency f_{ideal} of an unpinned vortex core. The average of the frequency shifts for a given disk is

$$\langle \Delta f_G \rangle = \frac{1}{N_{peak}} \sum (f_{\max} - f_{ideal}) = \langle f_{\max} \rangle - f_{ideal}, \tag{11}$$

where N_{peak} is the number of peaks. Frequency peaks are selected by the criteria of Sec. III H. Figure 12(a) shows the distribution of frequency maxima $f_{\max}$ extracted from gyrotropic frequency versus field data for 1-μm (open squares) and 2-μm (closed squares) SG disks.

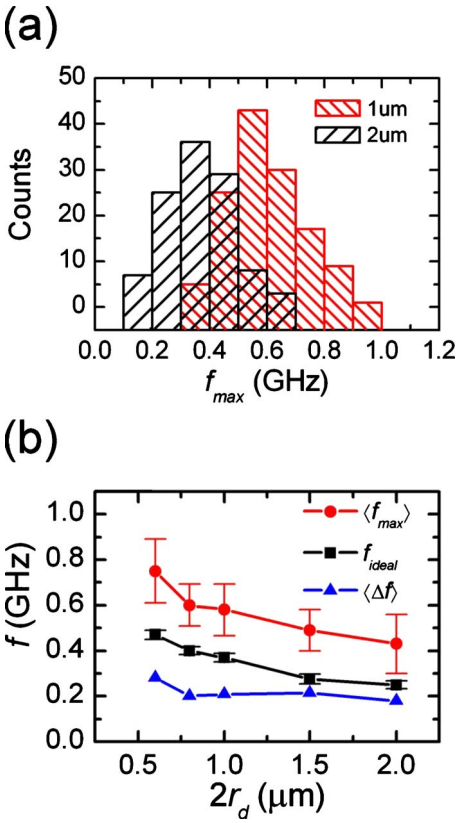

FIG. 12. (Color online) (a) Histogram of the distribution of frequency maxima for SG disks of 1-μm and 2-μm diameters. (b) The average frequency peak $\langle f_{\max} \rangle$ (red circles) is the average of the frequency maxima for each disk in (a). The ideal gyrotropic frequency f_{ideal} (black squares) is estimated from experimental data. Error bars on $\langle f_{peak} \rangle$ give the standard deviation while error bars on f_{ideal} give the standard error. The average frequency shift $\langle \Delta f \rangle = \langle f_{\max} \rangle - f_{ideal}$ (blue triangles).

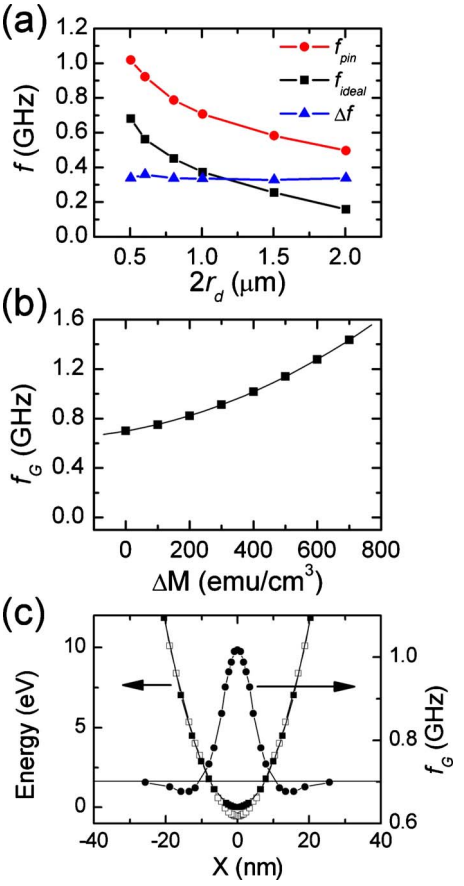

FIG. 13. (Color online) Results of micromagnetic simulations. (a) Gyrotropic frequency f_{ideal} of an ideal (unpinned) vortex (closed squares) and f_{pin} of a vortex with its core pinned by a defect (open squares) that is defined by a single $5\times5\times50$ nm^3 cell of reduced magnetization $M_{pin}=400$ emu/cm^3. The frequency shift due to pinning, $\Delta f_G = f_{pin} - f_{ideal}$, is shown using closed triangles. (b) f_{pin} of a pinned vortex as a function of $\Delta M_s = M_s - M_{pin}$. The solid curve is a fit to a second-order polynomial. (c) Energy as a function of the displacement X from the center of the disk for an ideal vortex (closed squares) and a pinned core (open squares). f_G as a function of X for the ideal vortex (horizontal solid line) and pinned core (solid circles).

Figure 12(b) shows $\langle f_{\max} \rangle$ (closed circles) as a function of disk diameter for the SG disks. Values for f_{ideal} (black squares), estimated from the experimental data, are shown for reference. The values for f_{ideal} were obtained by averaging the minimum frequency values in the data sets of frequency versus field. These values compare favorably to results from micromagnetic simulations. $\langle \Delta f \rangle$ (blue triangles), the difference between the average peak frequency and the ideal frequency, is approximately independent of disk diameter. Equivalent behavior was observed for the LG and XLG disks. Evidently the term in Eq. (10) that depends on disk diameter contributes negligibly to the frequency shift Δf_G. We conclude that $\Delta G_P \approx 0$ so that

$$\Delta f_G = \frac{\Delta k_P}{2\pi G_M} \tag{12}$$

and

$$W_P = \pi \Delta f_G G_M r_P^2. \tag{13}$$

We showed in Sec. III D that typical values of r_P are $\sim$20 nm. From Eq. (3), with typical values for Py, we estimate $G_M = 1.4\times10^{-9}$ ergs s cm^{-2}. Finally, with $\Delta f_G \approx 0.20$ GHz we have $W_P \approx 3.5\times10^{-12}$ ergs$=2.2$ eV.

It is significant that there appears to be an approximate upper bound for each diameter, which is only a factor of two higher than the unpinned frequency. In the context of the present argument, this limits the pinning energy associated with the defects, which in turn constrains the possibilities for the size and nature of the defects. Unfortunately, however, we have no specific information that would allow us to distinguish among possible origins such as local reductions in the saturation magnetization M_s or the exchange constant A. In the remainder of this paper, we will restrict our discussion to the simple case of a local reduction in M_s, which is an experimentally confirmed origin of strong pinning, including the extreme case of vortex core annihilation in disks patterned with a focused ion beam.[43]

I. Micromagnetic simulations

The foregoing results demonstrate that the frequency shift $\langle \Delta f \rangle$ is independent of disk diameter, suggesting that Δf depends only on the properties of the pinning defect and, in particular, on the pinning energy W_{pin}. For insight into the relationship between Δf and W_{pin}, we perform micromagnetic simulations using the LLG code.[37] Disks are defined on a 2D grid, with thickness 50 nm and diameters ranging from 0.5 to 2 μm. The cell size is $5 \times 5 \times 50$ nm^3. The magnetization is $M_s = 800$ emu/cm^3 and the exchange constant is $A = 1.3 \times 10^{-6}$ ergs/cm. A pinning defect is defined by changing the magnetization M_s of a single cell at the center of each disk. As shown in Fig. 13(a), the simulated frequency of the gyrotropic mode for a defect-free disk (open squares) scales inversely with disk diameter, as expected.[5,6] For a disk with a single cell defect magnetization of $M_{pin} = 400$ emu/cm^3, the same inverse dependence on disk diameter is seen (closed squares) but with a frequency shift Δf that is nearly independent of disk diameter (triangles), consistent with the experimental results in Fig. 12(b). In Fig. 13(b) we show the pinning frequency as a function of the difference $\Delta M_s = M_s - M_{pin}$ between the magnetization M_{pin} of the defect and the saturation magnetization M_s of the rest of the disk. Since the magnetostatic energy is quadratic in M_s, the strength of the pinning defect increases linearly at small ΔM_S, with a quadratic term for larger ΔM_S.

Figure 13(c) shows the magnetostatic energy in a 500-nm disk as a function of the displacement of the vortex core from its equilibrium position, with (open squares) and without (closed squares) a defect (single cell with $M_s = 400$ emu/cm^3) in the center of the disk. The core displacement is varied by application of a static field. The vortex gyrotropic frequency is obtained from the simulated response to an experimentally realistic Gaussian field pulse of amplitude 10 Oe and temporal width 150 ps applied in the sample plane. The horizontal line in Fig. 13(c) indicates the gyrotropic frequency for an ideal vortex. When the vortex core is centered on the defect, its frequency is shifted upwards relative to the ideal case. The width of the frequency peak compares to the region over which the pinned and unpinned energies differ. The amplitude and width of the frequency peak compare favorably with our experimental observations. Finally, we note that the pinned frequency curve has wings that dip slightly below the ideal line before approaching it again at large distances from the defect. Similar features are often observed experimentally but their interpretation is complicated by the close proximity of neighboring frequency peaks. These features are likely related to the out-of-plane magnetization distribution of the vortex core itself. In particular, the demagnetizing field from the central peak of the core magnetization distribution induces a ring of oppositely directed out-of-plane magnetization surrounding the core center. This feature is observed in micromagnetic simulations but has been observed experimentally only in the deformation that precedes core reversal.[44] Gyrotropic frequency data for a well-isolated defect might therefore be used to verify this feature of the vortex magnetization distribution.

IV. SUMMARY

In summary, we have demonstrated that pinning associated with intrinsic defects has a profound influence on the dynamics of magnetic vortices. For small excitation amplitudes, the field dependence of the gyrotropic mode frequency is governed by the density and strength of individual pinning sites. With increasing amplitude, a threshold excitation field is reached, beyond which the vortex core is depinned from the defect. We have shown that the average frequency shift due to pinning is independent of disk diameter. This observation provides a means for estimating a vortex/defect interaction energy of approximately 2 eV. The ability to extract quantitative information about the vortex/defect interaction suggests further uses of vortex core dynamics as a sensitive probe of magnetic microstructure. In particular, the ability to characterize individual defects would allow for the testing of microscopic models of macroscopic phenomena such as Barkhausen noise and magnetic hysteresis.

ACKNOWLEDGMENTS

This work was supported primarily by NSF under Grant No. DMR 04-06029, the NSF NNIN program through the Minnesota Nanofabrication Center, and the Minnesota Supercomputer Institute. We also acknowledge support of the University of Minnesota Materials Science and Engineering Center through NSF under Grant No. DMR-0819885. We thank Chris Leighton and Jeff Parker for assistance with sample preparation.

*crowell@physics.umn.edu

[1] J. Raabe, R. Pulwey, R. Sattler, T. Schweinböck, J. Zweck, and D. Weiss, J. Appl. Phys. **88**, 4437 (2000).
[2] M. Schneider, H. Hoffmann, and J. Zweck, Appl. Phys. Lett. **77**, 2909 (2000).
[3] T. Shinjo, T. Okuno, R. Hassdorf, K. Shigeto, and T. Ono, Science **289**, 930 (2000).
[4] A. Wachowiak, J. Wiebe, M. Bode, O. Pietzch, M. Morgenstern, and R. Wiesendanger, Science **298**, 577 (2002).
[5] K. Yu. Guslienko, B. A. Ivanov, V. Novosad, Y. Otani, H. Shima, and K. Fukamichi, J. Appl. Phys. **91**, 8037 (2002).
[6] J. P. Park, P. Eames, D. M. Engebretson, J. Berezovsky, and P. A. Crowell, Phys. Rev. B **67**, 020403(R) (2003); J. P. Park and P. A. Crowell, Phys. Rev. Lett. **95**, 167201 (2005).
[7] S.-B. Choe, Y. Acremann, A. Scholl, A. Bauer, A. Doran, J. Stöhr, and H. A. Padmore, Science **304**, 420 (2004).
[8] J. Raabe, C. Quitmann, C. H. Back, F. Nolting, S. Johnson, and C. Buehler, Phys. Rev. Lett. **94**, 217204 (2005).
[9] V. Novosad, F. Y. Fradin, P. E. Roy, K. S. Buchanan, K. Yu. Guslienko, and S. D. Bader, Phys. Rev. B **72**, 024455 (2005).
[10] X. Zhu, Z. Liu, V. Metlushko, P. Grütter, and M. R. Freeman, Phys. Rev. B **71**, 180408(R) (2005).
[11] K. Yu. Guslienko, X. F. Han, D. J. Keavney, R. Divan, and S. D. Bader, Phys. Rev. Lett. **96**, 067205 (2006).

[12] K. W. Chou, A. Puzic, H. Stoll, D. Dolgos, G. Schütz, B. Van Waeyenberge, A. Vansteenkiste, T. Tyliszczak, G. Woltersdorf, and C. H. Back, Appl. Phys. Lett. **90**, 202505 (2007).
[13] K. Yu. Guslienko and K. L. Metlov, Phys. Rev. B **63**, 100403(R) (2001).
[14] T. Uhlig, M. Rahm, C. Dietrich, R. Höllinger, M. Heumann, D. Weiss, and J. Zweck, Phys. Rev. Lett. **95**, 237205 (2005).
[15] H. Barkhausen, Z. Phys. **20**, 401 (1919).
[16] P. J. Cote and L. V. Meisel, Phys. Rev. Lett. **67**, 1334 (1991).
[17] S. Zapperi, P. Cizeau, G. Durin, and H. E. Stanley, Phys. Rev. B **58**, 6353 (1998).
[18] G. Durin and S. Zapperi, Phys. Rev. Lett. **84**, 4705 (2000).
[19] E. Puppin, Phys. Rev. Lett. **84**, 5415 (2000).
[20] D.-H. Kim, S.-B. Choe, and S.-C. Shin, Phys. Rev. Lett. **90**, 087203 (2003).
[21] A. Schwarz, M. Liebmann, U. Kaiser, R. Wiesendanger, T. W. Noh, and D. W. Kim, Phys. Rev. Lett. **92**, 077206 (2004).
[22] M.-Y. Im, S.-H. Lee, D.-H. Kim, P. Fischer, and S.-C. Shin, Phys. Rev. Lett. **100**, 167204 (2008).
[23] G. Meier, M. Bolte, R. Eiselt, B. Krüger, D.-H. Kim, and P. Fischer, Phys. Rev. Lett. **98**, 187202 (2007).
[24] S. Lemerle, J. Ferré, C. Chappert, V. Mathet, T. Giamarchi, and P. Le Doussal, Phys. Rev. Lett. **80**, 849 (1998).
[25] J. P. Sethna, K. A. Dahmen, and C. R. Myers, Nature (London) **410**, 242 (2001).
[26] H. Shima, V. Novosad, Y. Otani, K. Fukamichi, N. Kikuchi, O. Kitakamai, and Y. Shimada, J. Appl. Phys. **92**, 1473 (2002).
[27] G. S. D. Beach, M. Tsoi, and J. L. Erskine, J. Magn. Magn. Mater. **320**, 1272 (2008).
[28] R. L. Compton and P. A. Crowell, Phys. Rev. Lett. **97**, 137202 (2006).
[29] D. Bedau, M. Kläui, S. Krzyk, U. Rüdiger, G. Faini, and L. Vila, Phys. Rev. Lett. **99**, 146601 (2007).
[30] R. Moriya, L. Thomas, M. Hayashi, Y. B. Bazaliy, C. Rettner, and S. S. P. Parkin, Nat. Phys. **4**, 368 (2008).
[31] D. Bedau, M. Kläui, M. T. Hua, S. Krzyk, U. Rüdiger, G. Faini, and L. Vila, Phys. Rev. Lett. **101**, 256602 (2008).
[32] A. Vansteenkiste, J. De Baerdemaeker, K. W. Chou, H. Stoll, M. Curcic, T. Tyliszczak, G. Woltersdorf, C. H. Back, G. Schütz, and B. Van Waeyenberge, Phys. Rev. B **77**, 144420 (2008).
[33] G. Katz, Appl. Phys. Lett. **12**, 161 (1968).
[34] H. Bialas and E. Knoll, Vacuum **45**, 959 (1994).
[35] M. S. Lund and C. Leighton, J. Vac. Sci. Technol. A **22**, 2027 (2004).
[36] W. K. Hiebert, A. Stankiewicz, and M. R. Freeman, Phys. Rev. Lett. **79**, 1134 (1997).
[37] M. R. Scheinfein, LLG MICROMAGNETICS SIMULATOR, v.2.55 (2004). Simulations used a cell size of $5\times5\times50$ nm^3 and a Gaussian field pulse of amplitude 10 Oe and temporal FWHM 80 ps.
[38] V. S. Pribiag, I. N. Krivorotov, G. D. Fuchs, P. M. Braganca, O. Ozatay, J. C. Sankey, D. C. Ralph, and R. A. Buhrman, Nat. Phys. **3**, 498 (2007).
[39] A. R. Pereira, Phys. Rev. B **71**, 224404 (2005).
[40] W. A. Moura-Melo, A. R. Pereira, R. L. Silva, and N. M. Oliveira-Neto, J. Appl. Phys. **103**, 124306 (2008).
[41] A. A. Thiele, Phys. Rev. Lett. **30**, 230 (1973).
[42] D. L. Huber, Phys. Rev. B **26**, 3758 (1982).
[43] K. Kuepper, L. Bischoff, Ch. Akhmadaliev, J. Fassbender, H. Stoll, K. W. Chou, A. Puzic, K. Fauth, D. Dolgos, G. Schütz, B. Van Waeyenberge, T. Tyliszczak, I. Neudecker, G. Woltersdorf, and C. H. Back, Appl. Phys. Lett. **90**, 062506 (2007).
[44] A. Vansteenkiste, K. W. Chou, M. Weigand, M. Curcic, V. Sackmann, H. Stoll, T. Tyliszczak, G. Woltersdorf, C. H. Back, G. Schütz, and B. Van Waeyenberge, Nat. Phys. **5**, 332 (2009).